POLITECNICO
MILANO 1863

Space Propulsion Project

Martìnez Ferreira Daniel 10887367
Lima Augusto 10916450
Júnior Sávio 10880091
Scaramuzzino Alessio 10674740
Scarpa Edoardo 10664387
Torre Federico 10645141
Valsecchi Andrea 10677064
Viola Francesco 10680788
Zara Andrea 10698650

Course of Space Propulsion
School of Industrial Engineering
Academic Year 2022-2023

Abstract

In this paper a series of engines for a kick stage of a small satellite (250 kg of dry mass) are studied. The rocket has to grant a total Δv of 2500 m/s. A nominal thrust level of 500 N is selected. This value is doubled and halved in a successive analysis in order to compare a dimension variation in the engine. The process is repeated for two propellants couples: $N_2H_4 - NTO$ and $RP1 - H_2O_2$. The second is introduced in order to propose a *green* alternative to the *toxic* one. The engine shall be realized in additive manufacturing using compatible materials, both with the manufacturing techniques and with the adopted propellants. For the six engines are sized combustion chambers, injection plates and nozzles in addition to pressure-fed feeding lines. It is considered a cooling strategy for the engines with a combination of regenerative cooling, radiative cooling and thermal barrier coating.

Nomenclature

List of Symbols

Acronyms

NTO Nitrogen Tetroxide

HTP Highly Tested Peroxide

SRM Solid Rocket Motor

O/F Oxidizer to Fuel Ratio

LRE Liquid Rocket Engine

HRI Health risk index

UHTC Ultra-high temperature ceramic

SLM Selected Laser Melting

AM Additive Manufacturing

EBM Electron Beam Melting

CEA Chemical Equilibrium Applications

RPR Relative Roughnesses

RP-1 Rocket kerosen

TPMS Triply-Periodic Minimal Surfaces

RPR Pipe relative roughness

TBC Thermal Barrier Coating

CAD Computer-Aided Design

Symbol	Unit	Name
T	N	Thrust
P_c	bar	Chamber Pressure
I_s	s	Specific Impulse
I_v	gs/cm^3	Volumetric Specific Impulse
Δv	m/s	Variation of velocity
ρ	kg/m^3	Density
m_i	kg	Mass of i-specie
$\dot{m}_{p_i}$	g/s	Mass flow rate of the i-propellant
T_{boil}	K	Boiling temperature
D_e	mm	Exit diameter
D_c	mm	Chamber diameter
D_t	mm	Throat diameter
R_t	mm	Throat diameter
C_f	-	Thrust coefficient
P_{vap}	Pa, bar, MPa	Vapor pressure
L_{star}	mm	Characteristic length
L_{noz}	mm	Nozzle length
L_c	mm	Chamber length
θ_e	deg	Exit angle
θ_i	deg	Inlet angle
L_{conic}	-	Conic nozzle length
ε	-	Expansion ratio
ε_c	-	Contraction ratio
h_g	W/m^2K	Heat transfer coefficient
T_e	K	Adiabatic temperature
R	-	Recovery factor
T_f	K	Flame temperature
t_M	mm	Thickens of metal
T_I	K	Interface temperature
t_C	mm	Thickness of TBC
T_{wall}	K	Hot gas side wall temperature
$T_{radiative}$	K	Temperature of the external side of the radiative material
$\dot{Q}$	W	Total heat flux
$\dot{q}$	W/m^2	Total heat flux
ΔP	Pa, bar, MPa	Variation of pressure
v_i	m/s	Velocity of the i-fluid
D_{inj}	mm	Injector diameter
N_{holes}	-	Number of holes
Re	-	Reynolds number
f	-	Friction factor
Ma	-	Mach number
Ch/d	-	Chamfer size over biggest diameter

Contents

List of Figures

List of Tables

Chapter 1

Introduction

For the assigned mission the total dry mass is 250 kg, including both satellite and engine inert masses. The kick stage shall be able to provide a Δv of 2500 m/s. The engine shall be pressure-fed and the propellants shall be storable and not self pressurized. In order to select the thrust level and the main characteristics of the engine, motors from similar missions are analyzed.

1.1 Liquid Propellant Kick stage

A kick stage rocket motor for a satellite can be defined as any stage of a multistage rocket used to provide extra velocity to propel a spacecraft into its designated trajectory [1]. Starting from 1977, Aerojet Liquid Rocket Company began studying a *non-toxic* kick stage system to facilitate the operations of the ARIES payloads. The solution was a LRE built as a shortened version of Aerobee family with the goal of performing multiple short burns [2].

Nowadays, multi-injection capabilities are fundamental for deploying multiple payloads into their operational orbits. Skyrora is developing the third stage of *Skyrora XL* with a thrust up to 3.5 kN and a payload capability of 315 kg with respect to an orbit altitude of 500 km, capable of a much higher Δv compared to the mission case [3]. In accordance with the mission's design, the most similar mission is RocketLab's kick stage, in-house developed and manufactured, powered by the Curie engine [4], pressure-fed bipropellant thruster. It can transport up to 200 kg of payload and its motor, fully realized in additive manufacturing, can generate 120 N of thrust. It's main usage is to circularize and raise orbits from 500 to 1200 km altitude, therefore it provides a lower Δv than the one requested. According to the previous overview and supported by the reference [5], a thrust level of 500 N is selected.

This range is typical for bipropellant kick stages engines that operate with the propellant couple $N_2H_4 - NTO$ [6, 7, 8]. The reference engines have Chamber Pressure in the range of $7 - 11$ *bar* and Expansion Ratio between $100 - 300$. The chosen parameters for the engine are reported in Table 1.1.

Thrust [N]	Chamber Pressure [bar]	Nozzle Expansion Ratio
500	10	200:1

Table 1.1: Engine main parameters

Chapter 2

Propellant selection

2.1 Toxic Couple

The first propellant couple analyzed is Hydrazine and Nitrogen Tetroxide, whose characteristics are reported in Table 2.1.

Propellant	$\rho[g/cm^3]$	$P_{vab}[bar]$	$T_{boil}[C]$
N_2H_4	1.008	0.014	113.5
NTO	1.448	0.960	21.2

Table 2.1: Hydrazine and Nitrogen Tetroxide properties at ambient condition [9]

This couple is storable and gives high performances, but it is toxic and carcinogenic. Its performance is studied through the CEA code, assuming frozen expansion at the nozzle throat. The Specific Impulse is computed for a series of O/F values (Figure 2.1) in order to find the best mixture ratio for the propellants. The Design O/F is selected in the range of maximum Specific Impulse. Refining the analysis grid, the performances of the *Toxic Couple* are computed and reported in Table 2.2.
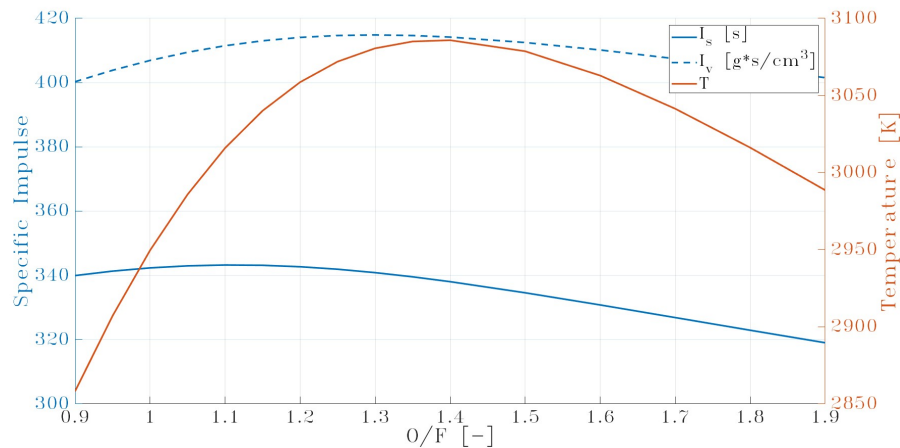
Figure 2.1: $N_2H_4 - NTO$ Performances with variable O/F ratio

O/F	I_s [s]	I_v [$g \cdot s/cm^3$]	$T_f[K]$
1.11	343	411	3016

Table 2.2: $N_2H_4 - NTO$ performances

2.2 Green propellant alternatives

In Figure 2.2 is shown the logic to chose the green propellants.
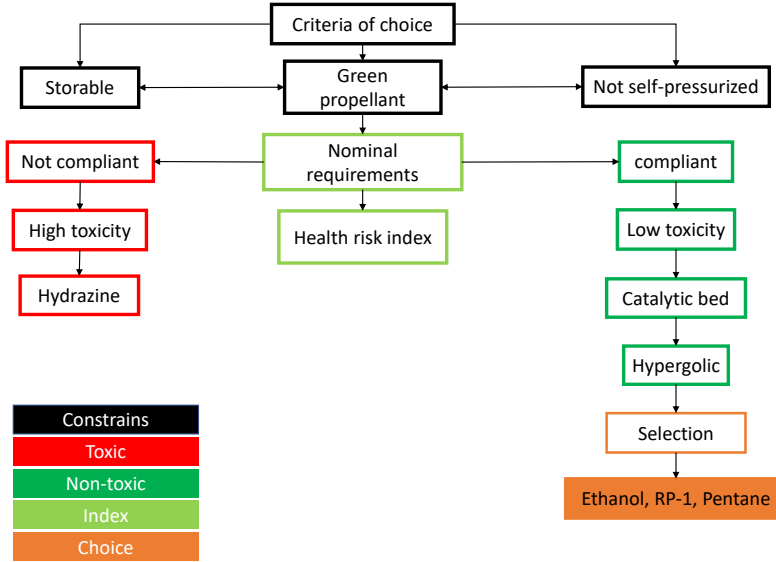
Figure 2.2: Propellant selection

The use of hydrazine and its derivatives like mono-methylhydrazine (MMH) and unsymmetrical dimethylhydrazine (UDMH) as propellants for in-space propulsion becomes increasingly more discouraged. Hydrazine is classified by the European Chemicals Agency (ECHA) as a substance that "may cause cancer" [10]. The main parameter for green propellant classification is the HRI that gives an idea about how much "green" is the propellant. The propellants, to be defined as "green", must satisfy specific requirements [10]. Different categories of fuels has been investigated: Nitro compounds, Boron, Lithium and Beryllium Based Propellants, hydrocarbons - that in turn can be divided in alkanes, alkenes and alkynes - and alcohols. By considering storable fuels, Hydrogen Peroxide (H2O2) as oxidizer and not self-pressurized propellant, the available choices are reported in Table 2.3.

Fuel	$\rho[g/cm^3]$	$P_{vap}[bar]$	HRI
Ethanol	0.79	5.7	0.15
RP-1	0.807	-	4.6
Pentane	0.63	0.57	4.6
Propanol	0.81	0.0199	0.029
Butanol	0.81	0.06	0.075
Pentanol	0.81	0.04	0.029
Pentyne	0.71	0.47	??

Table 2.3: Green fuels properties trade-off

3

For the family of alkanes, only Pentane is liquid at ambient condition; for alkynes only Pentyne is not self-pressurized, but this types of fuel present reactivity issues and could lead to problems such as explosions [9, 10]. For the alcohols: Ethanol, Propanol, Butanol and Pentanol are not self-pressurized, but, among these fuels, only Ethanol has been selected, since the other options are generally not used at this level of technology. To improve the flammability of the propellant, a catalytic bed or a catalyst [11] may be added.

2.3 Green couples trade-off

Among the remaining fuels presented in Table 2.3, the propellant couple selection is based on the theoretical performances with HTP, obtained with the CEA code. The different couples have been compared in terms of Specific Impulse (Gravimetric and Volumetric) and Combustion Chamber Temperature. In the CEA code, the expansion is considered frozen at the nozzle throat. The performances are analyzed over a range of O/F values in order to identify the maximum Specific Impulse for each couple. In Figure 2.3, the performances of the fuels are reported.

(a) I_s $[s]$ and I_v $[g \cdot s/cm^3]$

(b) T_f $[K]$
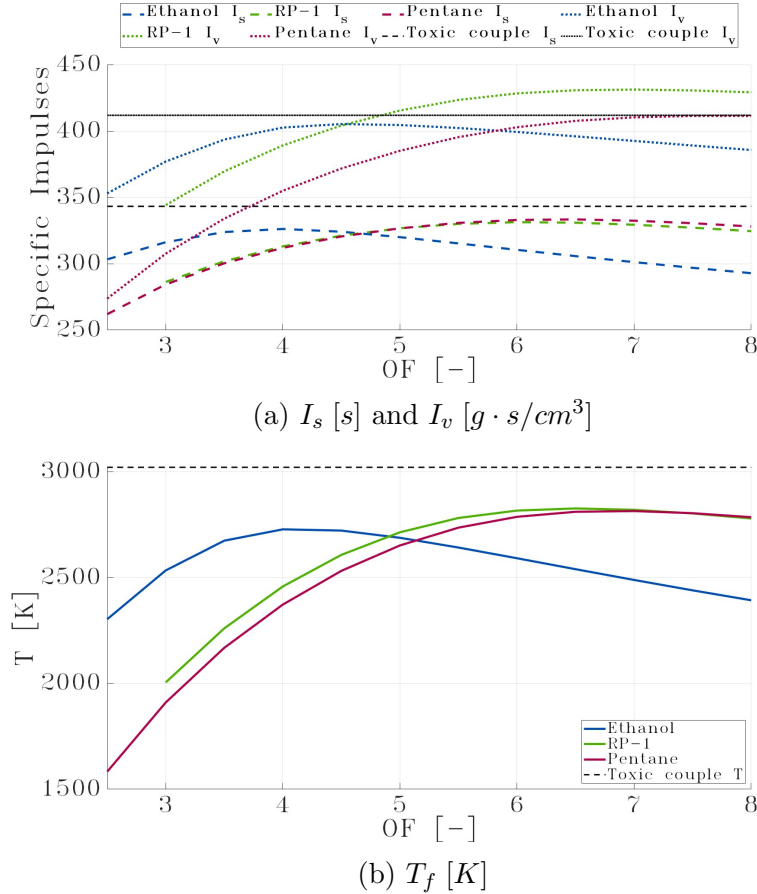
Figure 2.3: Green propellants performances

Comparing with the toxic couple's performances, the best fuel is Pentane in terms of Specific Impulse (maximum for an O/F ratio around 6). However, this fuel is characterized by a very low density, therefore the Volumetric Specific Impulse is much lower than the one of Hydrazine and NTO. The chosen propellant for the next engine sizing is *RP-1*, that shows a performance, reported in Table 2.4, comparable with the toxic couple in terms of, both I_s and I_v.

O/F	$I_s[s]$		$I_v[gs/cm^3]$		$T_f[K]$	
6.11	331	-4%	428	+4%	2817	-7%

Table 2.4: $RP-1-H2O2$ performance

The Thermo-chemical properties of the *green* couple are written in Table 2.5.

Propellant	$\rho[g/cm^3]$	$P_{vap}[bar]$	$T_{boil}[C]$
RP-1	0.807	-	187
HTP	1.437	0.007	148

Table 2.5: RP-1 and Hydroge Peroxide properties at ambient condition [9, 12]

2.3.1 Catalytic bed

The tree diagram represented in Figure 2.4 shows the followed logic for the selection of the catalytic bed.
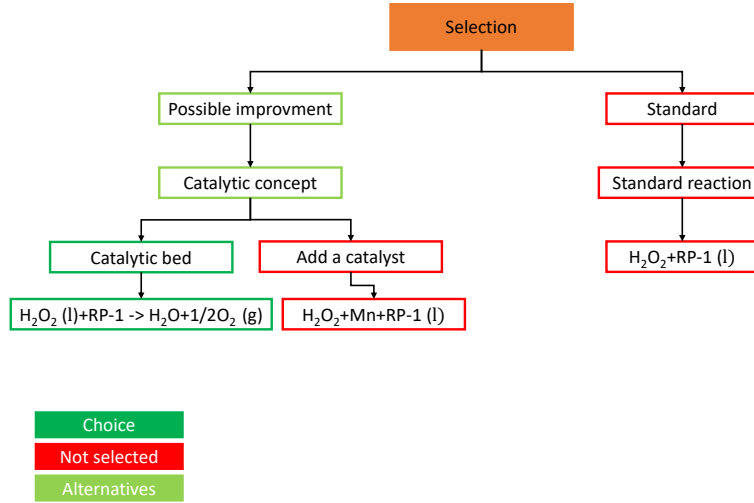
Figure 2.4: Catalytic bed selection

When Hydrogen Peroxide is used as an oxidizer, there are generally three methods for fuel combustion: the first one considered is the "standard" case, which uses only one injection plate and does not consider any previous chemical transformation of the propellants. The second method is referred to as staged-bipropellant combustion and uses decomposed Hydrogen Peroxide, which is obtained from a catalytic bed reaction that gives oxygen and water vapor, releasing high thermal energy [13]. This improves the mixing between fuel and oxidizer, and, as a result, better flammability of the propellant is achieved. The third one consists in dissolving a catalyst in the fuel [11]. These materials are noble metals, such as Platinum, Silver or Manganese [13]. In our study, Manganese is considered due to its superior reactivity [13], increasing the flammability of the mixture but reducing the performances for the presence of a condensed phase. However, in the case of RP-1, even with 10% of additive, the flammability is not completely spontaneous [11], but needs an igniter to combust the mixture. The behavior of this different configuration is

modeled using NASA CEA computation. The comparison is performed in terms of Specific Impulse (Figure 2.5). Starting from this consideration, the catalytic bed configuration is chosen.
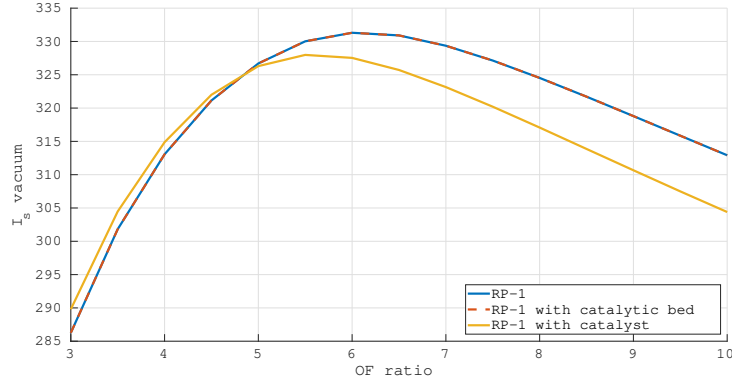
Figure 2.5: RP-1 with not decomposed and decomposed H_2O_2, and with catalyst (10% Mn)

In Figure 2.5, the selected catalytic bed configuration for the green propellant engine [14] is displayed. The catalytic bed traditionally used for Hydrogen Peroxide decomposition is a silver-plated nickel or stainless steel mesh. So-called "structured" catalysts have the potential to promote fluid turbulence while also maintaining a low pressure drop.
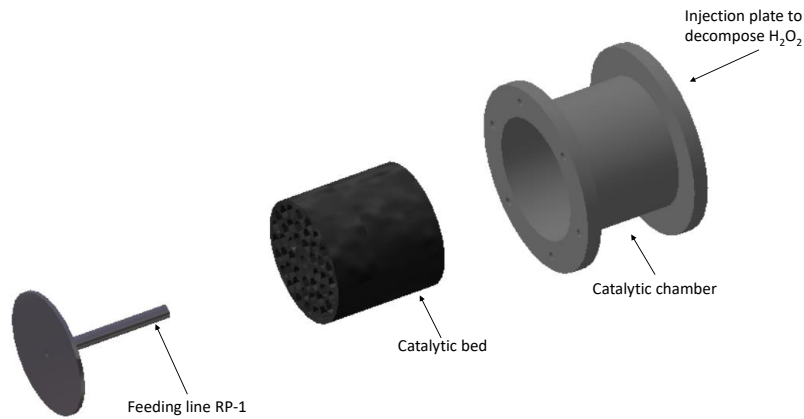
Figure 2.6: CAD model catalytic bed

As shown in Figure 2.6, the configuration with catalytic bed is quite different with respect to the "standard" case. This model includes a first injector for H_2O_2, the catalytic bed, the feeding line for the fuel, and finally the injection plate to mix the fuel and oxidizer already decomposed.

The sizing of the injection plate will be discussed in Section 4.4.1, while the dimensions of the catalytic bed are reported in Section 4.1. Catalysts used to induce hydrogen peroxide decomposition are often plagued by low melting point and high pressure drop. 3D-printing may offer solutions to many of these issues, through the realisation of complex geometries such as triply-periodic minimal surfaces (TPMS). From [14] *Platinum* (H2PtCl6) emerged as the most active catalyst. An important characteristics of this catalytic bed is that Alpha alumina is chosen as the catalyst support material, since this

material exhibits appropriate high temperature and mechanical properties for the targeted application, with operating temperatures ranging from 500 ℃ to 1000 ℃ and relatively fast thermal cycles.

Chapter 3

Materials

3.1 Material Compatibility with Mission

Upon a short literature survey regarding possible additive manufacturing materials, a final list of possibilities was built, taking into account reliability (use on previous missions) and thermomechanical properties.

Ti-6Al-4V is a Titanium alloy that has been used on Selective Laser Melting and Electron Beam Melted manufacturing processes successfully for the last decade for aerospace applications with high thermomechanical stresses [15], with its potential highlighted for in-space propulsion applications [16]. Indeed, even when submitted to the additive manufacturing processes mentioned, the material holds the high mechanical properties of the bulk alloy [17]. Furthermore, the material has compatibility with Hydrazine [18]. The drawback relies on the fact that no previous records of applications for space propulsion combustion chambers were found, so the material lacks actual practical reliability, although many papers and references indicate its potential for in-space propulsion applications.

INCONEL 625 is a Nickel-chromium-molybdenum alloy, that has been used for the production of combustion chambers, injectors and nozzles of engines built using additive manufacturing processes. In particular, its higher level of molybdenum gives the alloy a remarkable resistance against corrosion. Moreover, Inconel 625 maintains its high mechanical strength up to temperatures around 923K [19]. There are also examples of successful hot-fire tests of engines composed by SLM printed Inconel 625 showcased [19]. Beyond that, it is also compatible with Hydrazine [18].

INCONEL 718 is another Nickel-chromium-molybdenum alloy, but differently from its counterpart, it has a higher concentration of iron instead of molybdenum, making it more strength focused [20]. As Inconel 625, it also has a record of successful hot-fire tests conducted on engines that contained injection plates and combustion chambers made of SLM printed Inconel 718, anit also maintains its high mechanical strengths up to temperatures around 923K [19]. Despite having superior mechanical performance than its 625 counterpart, no data has been found regarding its compatibility with Hydrazine [18].

Table 3.1 contains a summary on the quantitative properties of interest of the materials presented.

Name	INCONEL 718	INCONEL 625	Ti-6Al-4V
Thermal conductivity [W/m.K]	11.4	9.8	8.0
Specific Heat [J/Kg.K]	435	410	570
Melting Point [K]	1533	1563	1877
Max Operating Temp [K]	923	923	1073
Density [kg/m^3]	8900	8440	4430
Max Stress (@MaxTemp) [MPa]	900	700	400
Compatibility with Hydrazine	NO DATA	YES	YES

Table 3.1: Properties of potential materials

Therefore, due to its considerable reliability (having been used in previous successful liquid propulsion systems in the past), high performance under critical temperature conditions and assured compatibility with Hydrazine, Inconel 625 was the material selected for the injection plate and combustion chamber's manufacturing.

3.2   Additive Manufacturing and Accuracy Limits

Additive manufacturing can produce complex features that are not possible with traditional manufacturing techniques. In general AM processes can be divided into three main categories [19]: Powder Bed based, Direct Engine Deposition and Solid State.

The resolution of the features are notably higher for Powder Bed based processes [19], such as Selective Laser Melting (SLM) and Electron Beam Melting (EBM).

After a literature review from both processes, the SLM process is then chosen, due to its capability of producing metal parts from the Inconel 625 of high geometrical complexity [21].

For the manufacturing of this particular manufacturing process, the SLM800 printer [22] is chosen, since it has a sufficient envelope size to print the thruster in one block. Its specific properties are shown in Table 3.2.

Building Envelope [mm]	Minimum Feature Size [μm]	Build Rate [cm^3/h]	Minimum Layer Thickness [μm]
500 x 280 x 875	150	up to 171	20

Table 3.2: SLM800 Technical Specifications

Additionally, a limitation on the slope angle of inclined sections must be included so that during printing, different layers with increasing width are correctly stacked (and they stick) on top of the previous layer. Overhangs are the biggest thing to avoid, which means that the printing process of the rocket engine should begin from the injector plate, continue with the combustion chamber, then the throat and finally the nozzle. This is so that the case can be printed in a single operation.

To simulate the printing process, the slicing software UltiMaker Cura [23] was used. Custom versions of the SLM800 Printer [22] and the Inconel 625 [24] powder were added to the software's library as to model the printer's capabilities. Infill option of 100% and the possibility of printing supports to help during the manufacturing was allowed. Figure 3.2 shows the preview of the Nominal Toxic Propellant Engine's printing process. Similar slicing simulations have been performed for the other versions. Also, an expected time of 10 days for the complete printing of each model was obtained, as seen in Figure 3.1.

10 days 15 hours 23 minutes

6109g · 113.46m

Figure 3.1: Expected printing time for the Nominal Toxic Propellant Engine's piece, taken from UltiMaker Cura's software [23].

As it can be seen, the dimensions of the motor fitted the maximum printable dimensions of the SLM800 and only a base support (represented in blue) was added to the printed piece. This proves the design's printability and the lack of long supports also reduce the need of additional post-processing procedures.
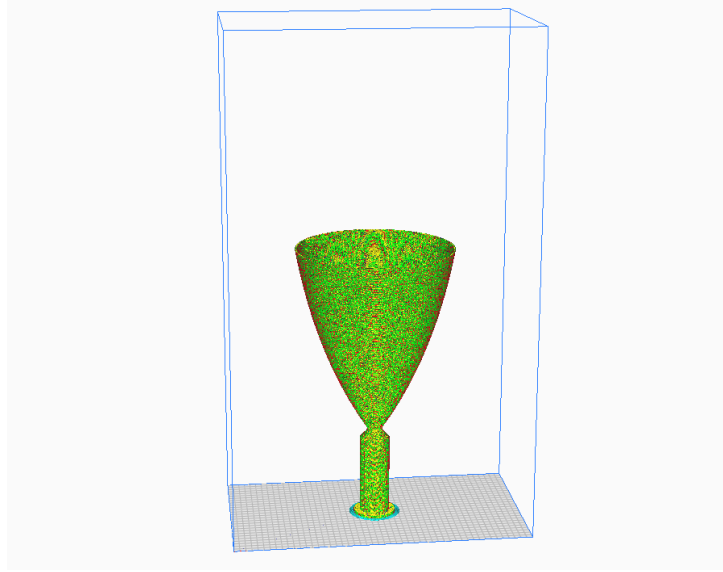
Figure 3.2: Preview of Nominal Toxic Propellant Engine's printing process using Ulti-Maker Cura's software [23]

3.3 Cooling system materials

Thermal Barrier Coating

In order to decrease the temperature on the internal surface of the engine case, a TBC is applied. It is a ceramic material with low conductivity and high thermal resistance. This type of materials are defied as Ultra-high temperature ceramics (UHTC) and are material defined as having an high melting point (around 3000 °C), a working range temperature around 2000 °C and very low thermal conductivity [25]. This group of ceramics is made up of carbides, borides and some nitrides of group four and five transition metals (Ti, Zr, Hf, V, Nb and Ta) [25]. At this stage it has been selected the ZrO_2 as material for TBC. The data of this material are reported in Table 3.3 [1]

Radiative Cooling

In the final part of the divergent nozzle the only form of cooling is from radiative source. In order to improve the heat transfer the divergent wall is realized with a different material.

---

[1]This data are retrieved form software *Grenta EdupPack 2021 R2, ANSYS Inc.*

	Zirconium oxide (ZrO_2)
Melting Point [°C]	2700
Max service temperature [°C]	2150 - 2250
Thermal conductivity [W/mK]	1.7 - 2
Typical uses	Structural application, engine and turbine parts

Table 3.3: Zirconium Oxide thermal properties

The best materials [26, 27] for this application are:

- *Niobium C103 coated with fused Silica*, frequently used for nozzle radiative cooling [28, 29, 30].

- *Iridium-coated Rhenium*, that is still in developing [31].

- *Tantalum-Tungstenum alloy*, that has a high thermal resistance but lower emissivity [32].

The main properties for the material of choice are reported in Table 3.4 [2] .

Name	Ta-10W
Maximum Service T [K]	1643-2753
Thermal Conductivity [W/mC]	34-52
Emissivity (@ 2000K)	0.302

Table 3.4: Main properties of Tantalum-10%Tungsten (Ta-10W)

---

[2]This data are retrieved form software *Grenta EdupPack 2021 R2, ANSYS Inc.* and [32]

Chapter 4

Engine sizing

In this section, the results of the engine sizing are presented. The sizing goes through the design of chamber, nozzle and the injection plate and the cooling system for the nominal engines. Moreover, in the end also a comparison between the upscale and downscale is presented.

4.1 Combustion chamber

The key point in the sizing of the combustion chamber is the choice of the characteristic length. The values chosen for the two propellants are reported in Table 4.1.

	NTO/N_2H_4	$HTP/RP-1$
L_{star} [m]	0.762	0.950

Table 4.1: L_{star} selection

The choice of the characteristic length for the couple HTP/RP-1 is based on the fact that the entering mixture in the combustion chamber is composed by H_2O and O_2 in gaseous form at high temperature. That means the mixture is very reactive and the value of L_{star} can be reduce to the minimum value used in literature [13]. However, a catalytic chamber must be add before the combustion chamber; the size of that are fix to $35mm$ of length and the diameter is the same of the chamber diameter [13], [33]. Moreover, the size of all the engine is done assuming a chamber mach number equal to 0.1.

4.2 Nozzle design

The design of the nozzle is strongly dependent on the expansion ratio, however the design's printability was also considered. In fact, the size of the engine is constrained to be compatible with the printable volume reported in Table 3.2.
The nozzle for all the engines are designed according to the *Rao nozzle contour* with the parameter reported in Table 4.2 [34, 35].

θ_e [deg]	θ_i [deg]	$\%L_{conic}$
34	10	0.7

Table 4.2: Parameters used for bell nozzle

4.3 Engine cooling

4.3.1 Preliminary Analysis

One of the preliminary steps in the design of a rocket engine cooling system is the analysis of the heat transfer from the combustion chamber to the chamber walls. The heat transfer occurs mainly through forced convection; the determination of the gas-side heat transfer coefficient h_g is a rather complex problem. The difference between the several analytical model are related to the initial assumptions for the calculation. In the following design the *Barz* model is adopted [36].

A preliminary analysis up to the throat is performed, the divergent section is instead analyzed separately. All values required for convective coefficient determination are taken from NASA CEA code with frozen expansion at the throat. The combustion chamber area is considered as infinite.

In proximity of the internal walls of the engine, the propellant velocity is lower with respect to the centre of the control volume, therefore for the heat transfer analysis the adiabatic temperature is exploited (T_e), which is obtained by multiplying the total temperature of the propellant and the recovery factor (R) [36]. Knowing T_e and imposing T_{wall}, it is possible to compute the specific heat flux ($\dot{q}$) that should be dissipated through the selected design. T_{wall} is set equal to 923 K, which is the maximum service temperature for the Inconel 625. These considerations are assumed for both *toxic* and *green* designs. In the preliminary analysis, only 2 points are taken into account: chamber and throat (where $\dot{q}$ is maximum). The parameters are retrieved from CEA only in this two section and the thermal analysis is performed. Through the midpoint integral it is then possible to compute the heat flux ($\dot{Q}$). The lateral areas required are recovered from the CAD model. Note that the throat area is defined from a contraction ratio of 5.77 for the *toxic* engine (5.878 for *green* engine) to an expansion ratio of 5.77 (5.878 for *green* engine). Regenerative cooling is adopted as the cooling solution in the attempt of achieving maximum performance.

NTO	N_2H_4	HTP	RP-1
369	387	373	460

Table 4.3: Maximum temperature of the coolants [K]

For this study some assumptions are introduced. The initial $T_{coolant}$ is set equal to 298.15 K and a pressure of 18 *bar* is considered in the feeding line. The external walls of the chamber and the nozzle are fixed at max temperature showed in Table 4.3. The maximum temperature of NTO is given as the temperature of boiling at 18 bars, due to the thermodynamic model [37]. For Hydrazine and RP-1, the maximum temperatures are taken as the boiling temperatures at 1 bar, assuring that the coolant cannot change phase, since the boiling temperature increases with a higher pressure. It is important to avoid the dissociation of Hydrogen Peroxide, because it is an exothermic reaction. To make a conservative assumption, the boiling temperature of water is considered, which is lower than the boiling temperature of HTP.

As shown in Table 4.4 all possible combination increase too much the coolant fluids' temperature. To solve this problem, a layer of ceramic material of 0.1 *mm* is introduced in the internal part of the nozzle. However, in this case the assumptions taken for the thermal model change. The temperature of the internal part of the ceramic layer is now fixed at 2200 K according to Section 3.3. Instead the T_{wall} is not constant, it should be monitored and kept under 923 K. Results are shown in Table 4.5.

Temperature without Ceramic [K]		NTO / N_2H_4			HTP / RP-1		
Thrust size		250N	500N	1000N	250N	500N	1000N
Chamber and Throat	O	298.15	298.15	298.15	298.15	298.15	298.15
Fuel	F	980.63	766.13	618.06	3434.5	2965.5	2424.3
Chamber Fuel	O	780.24	745.48	556.69	642.88	602.74	593.47
Throat Oxidizer	F	706.25	511.13	468.29	2017.7	1672.6	1210.5
Chamber Oxidizer	O	1038.3	688.30	611.44	716.63	625.04	520.12
Throat Fuel	F	562.38	543.00	437.77	1714.8	1581.0	1601.8
Chamber and Throat	O	1530.6	1145.8	880.13	1061.5	939.77	815.59
Oxidizer	F	298.15	298.15	298.15	298.15	298.15	298.15

Table 4.4: Preliminary thermal analysis

Temperature with Ceramic Coating [K]		NTO / N_2H_4			HTP / RP-1		
Thrust size		250N	500N	1000N	250N	500N	1000N
Chamber Fuel	O	440.25	435.54	371.10	386.98	369.21	374.24
Throat Oxidizer	F	423.21	363.06	346.28	758.71	658.91	542.45
Chamber Oxidizer	O	530.57	422.66	392.56	410.15	378.29	357.50
Throat Fuel	F	372.9	370.24	334.32	663.54	621.60	611.18

Table 4.5: Preliminary thermal analysis with thermal coating

In order to obtain a more accurate model, an in depth analysis is performed, dividing the throat into 16 sections. The length between the beginning of the convergent and the divergent with expansion ratio of 5.77 (5.828 for *green* couple) is divided in 17 points. For each couple of consecutive points is computed the area using the CAD model and the heat flux is computed in the mid point (Figure 4.1). In this way exploiting the midpoint integral, the throat heat flux is less overestimated and the previous unfeasible case can become achievable. Results are reported in the following Sections 4.3.2, 4.3.3.
It is important to notice that the aim of this chapter is to complete a global analysis; all heat is exchanged at once and no intermediate variation in the coolant fluid temperature is considered. Structural analysis and accurate sizing of the cooling channels are not part of this report.

4.3.2 Hydrazine 500N engine

As shown in Table 4.5 the best preliminary case is to cool the chamber with the fuel and the throat with the oxidizer. This choice is based on the fact that no intermediate points are considered for the combustion chamber, therefore the preliminary estimation is exactly the same of the more in depth analysis. If the coolant temperature in the chamber is over the constraint it is possible to conclude that the case is unfeasible and no more investigation is required.
Instead, in the case selected, the temperature of the fuel (chamber cooling fluid) at the end of the thermal exchange remains under the maximum temperature admissible at the pressure of 18 *bar*.
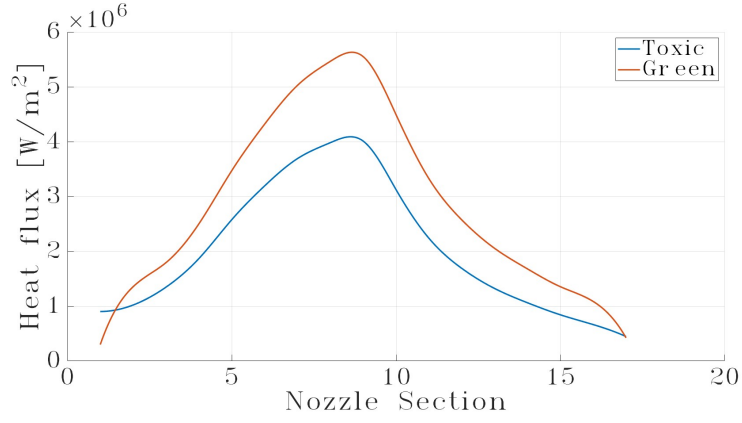
Figure 4.1: Heat flux for the two engines, the nozzle point are obtained from the discretization

	Chamber	Convergent						
ε	5.77	5.029	3.691	2.560	1.776	1.3833	1.157	1.0362
t_M [mm]	5.81	5.17	3.87	2.82	1.95	1.49	1.32	1.26
T_I [K]	921.82	908.18	901.71	906.68	881.83	855.37	867.46	881.98
t_C [mm]	2.35	2.10	1.60	1.15	0.85	0.70	0.60	0.55

Table 4.6: Thickness of ceramic and metallic wall and the interface temperature in chamber and convergent regenerative cooled in NTO-Hydrazine engine 500N

	Throat	Divergent						
ε	1	1.177	1.547	1.965	2.426	2.932	3.584	4.405	5.301
t_M [mm]	1.23	1.61	2.40	2.95	3.82	5.08	6.23	8.10	10.08
T_I [K]	872.49	882.70	918.32	877.49	885.87	920.11	905.30	918.79	921.90
t_C [mm]	0.55	0.70	0.95	1.30	1.65	2.00	2.55	3.20	3.95

Table 4.7: Thickness of ceramic and metallic wall and the interface temperature in throat and divergent regenerative cooled in NTO-Hydrazine engine 500N

As expected, the final temperature of the oxidizer ($T_{fin\,OX}$) decrease to 357 K, below its temperature of boiling (Table 4.3) while $T_{fin\,FUEL}$ is equal to 373.06 K, exactly as shown in Table 4.5. Due to the assumptions adopted in section 4.3.1, the thickness of the walls change along the axial direction, according to the different heat flux, as shown in Table 4.6, 4.7. Moreover the ceramic layer thickness is considered variable, in order to keep the metallic layer temperature below the limit imposed. The operational idea is to define the minimal thickness value from a minimum of 5×10^{-5} mm that allows to get a feasible solution. As shown in the Tables 4.6, 4.7, the thickness of ceramic layer oscillates between 3.95 mm and 0.55 mm while the thickness of metallic layer oscillates between 10.08 mm and 1.23 mm. The values obtained are feasible for minimal 3D printing requirements.

4.3.3 RP1 500N engine

As shown in Table 4.5 for the *green couple*, the best preliminary case is to cool the chamber with the fuel and the throat with the oxidizer. The case-selection drivers are the same explained in section 4.3.2. In particular, it is possible to see that the temperature of the

fuel is too high, while H_2O_2 is respecting its constraints with some margin. For this design, theO/F ratio is 6.11 therefore the oxidizer, also due to its good thermal capacity (being similar to H_2O) should be widely used for refrigeration. Because of this considerations, the cooling system effort for the combustion chamber is partitioned between $RP-1$ and H_2O_2. In the solution adopted, the oxidizer provide a cooling effect on half of the the chamber and all the length of the throat. The temperature of the internal wall of the ceramic layer, instead, is now fixed at 1800K. This assumption is related to the fact that an high T_{wall} is now not required due to the improved cooling performances. The lower the temperature is fixed, the thinner the walls would be.

The solution obtained is feasible and both the coolant fluid temperatures respect the constraints: $T_{finOX} = 357.75$ K; $T_{finFUEL} = 373.06$ K. It can be noticed that for the T_{finOX} we are really close to the boundary imposed. According to literature, H_2O_2 as oxidizer should be treated carefully due to its exothermic dissociation. However, it should be taken into account that the maximum admissible values for $RP-1$ and H_2O_2 4.3 refers to the ambient pressure, while in the feeding line the estimated pressure is above 15 bar. Therefore the limit temperature increases and the solution founded is acceptable.

	Chamber		Convergent						
	O	F							
ε	5.828		5.088	3.721	2.568	1.776	1.383	1.155	1.036
t_M [mm]	1.23	17.78	3.69	2.89	2.13	1.44	1.22	1.05	0.83
T_I [K]	917.43	917.43	883.24	902.81	917.42	881.53	911.03	913.18	835.73
t_C [mm]	2.50	5.00	1.15	0.85	0.60	0.45	0.35	0.30	0.30

Table 4.8: Thickness of ceramic and metallic wall and the interface temperature in chamber and convergent regenerative cooled in RP1-HTP regenerative cooled engine 500N

	Throat	Divergent							
ε	1	1.178	1.549	1.966	2.429	2.936	3.595	4.432	5.344
t_M [mm]	0.79	1.09	1.61	1.97	2.48	3.13	3.97	4.80	5.90
T_I [K]	820.47	874.91	919.57	891.48	893.49	910.49	922.75	905.30	909.25
t_C [mm]	0.30	0.35	0.45	0.60	0.75	0.90	1.10	1.40	1.70

Table 4.9: Thickness of ceramic and metallic wall and the interface temperature in throat and divergent regenerative cooled in RP1-HTP regenerative cooled engine 500N

Tables 4.8, 4.9 show the variable thickness of the the ceramic layer, the nozzle thickness and the temperature from the chamber to the throat.

4.3.4 Divergent part of the nozzle

The divergent section is approached in a different way and its solution is common and applied to all engines. Radioactive heat transfer analysis is performed. The coating layer is no more required, however the material for the divergent section is different. The final choice fell on Tantalum - Tungsten Alloy [32] due to its high temperature resistance 3.3. The thickness of the nozzle walls are now fixed and equal to 1 mm while the T_{wall} should be monitored. Forced convection is still the major contributor in heat exchange inside the nozzle therefore the Barz model is adopted. In order to compute the final T_{wall} and verify the feasibility of the design with the Barz temperature dependent coefficient, a non linear system is solved. Near the throat, at expansion ratio equal to 5.301 (5.9 for the

green couple), the heat flux is the highest in the whole divergent. Therefore this point if the temperature reached is inside the constraints, then for sure all the remaining point will be feasible and the solution found acceptable. The results are shown in Tables 4.10 4.11.

ε	5.301	10	25	100	200
T_{wall} [K]	2271.69	2066.04	1761.38	1330.59	1142.82
$T_{radiative}$ [K]	2263.11	2060.14	1758.26	1329.57	1142.26

Table 4.10: Divergent wall temperature for the *toxic* couple engine [K]

ε	5.344	10	25	100	200
T_{wall} [K]	2241.03	2064.43	1790.01	1384.57	1200.98
$T_{radiative}$ [K]	2232.90	2058.55	1786.67	1383.37	1200.30

Table 4.11: Divergent wall temperature for the *green* couple engine [K]

4.3.5 Engine Upscaling and Downscaling

As it is highlighted in Tables 4.4 and 4.5 when the thrust increases the cooling capabilities increase as well. As the thrust increases, the mass flow rate of propellant also increases proportionally, assuming an optimal nozzle. This means that more heat can be stored in the liquid propellant. However, the heat that needs to be stored does not increase at the same rate, but rather increases with the square root of the thrust, as shown in 4.2. Assuming that the wall temperature T_{wall} and the gas

Figure 4.2: $\dot{Q}$ variation with Thrust

temperature T_e are constant, we can derive an expression for the total heat flux $\dot{Q}$ as a function of the nozzle throat radius R_t. Due to Barz model $h_g \propto R_t^{-0.2}$. The nozzle side area A_{side} is approximately proportional to R_t, so we have $\dot{Q} \propto R_t^{0.8}$ Finally, with the thrust coefficient equation, we can relate the thrust T to the throat radius: $T = C_f P_c \pi R_t^2$ Assuming that C_f is constant, we get $R_t \propto T^{0.5}$ Therefore, we can conclude that for a constant wall temperature and gas temperature, the total heat flux is approximately proportional to the square root of the thrust.

Propellant	N_2H_4 /NTO		RP1/HTP	
Thrust level [N]	250	1000	250	1000
$\dot{Q}$ [kW]	10.5 - 15.6	28.1-47.6	8.8 - 13.2	24.3 - 39.6
Maximum $\dot{Q}$ [kW]	14.2	56.8	9.8	39.3

Table 4.12: Estimated values of power absorption in up and down scaling

In Table 4.12 are reported the estimated values for the total power to be absorbed by the fuel. The maximum heat that the propellants can withstand is compared with an underestimated value, computed considering the heat flux to be equal to the exit value in

the section at expansion ratio of 5.77 (5.8 for *green* propellant). While the overestimated value is obtained considering the throat heat flux to be constant over the whole nozzle throat. With respect to the main cases, the small engines are more difficult to be cooled only with regenerative approach. Film cooling can increase the cooling capacity of small engines, but it also reduces the performance because some of the propellant does not participate in the combustion. Therefore, it is suggested to use a film cooling in order to reduce the heat to be absorbed, as frequently used in small engines [33]. Instead for the 1000 N thruster the regenerative cooling is more feasible, in fact even the overestimated values are compatible with the maximum amount of heat.

4.4   Injector plate

4.4.1   Injector sizing

The first step when designing the injector plate is guaranteeing mass continuity. By doing so, the number and size of injector holes can be defined. The first step was to define the type of injector plate; for an hypergolic couple like NTO and N_2H_4 the *like on like* impingement is the best choice in order to do not stress the plate over the limit from a thermal point of view. On the other hand, according to Section 2.3.1, for the *green* couple it has been chosen a shower head injector for the infusion of the HTP in the catalyst chamber and a triplet configuration for the second plate. These choice are guided from the fact that is not required a strong atomization for the first injection, instead, for the second one a good mixing between fuel and oxidant decomposed is necessary.
The number of injector holes was calculated by computing the maximum even number of holes so that the hole diameter is as small as possible without going below the additive manufacturing limits. This minimization of the size allows for better atomization of the propellants. As discussed in Section 3.2, some limitations on the sloping of the surfaces must be introduced. Luckily, the impingement angle requirement (along with other geometric characteristics, shown in Figure 5.2) are compliant with the additive manufacturing requirements, as well as other requirements such as a Ch/d higher than 2 and impingement distance equal to $5 - 7$ times the jet diameter [38].

In Table 4.13 are reported the characteristic of the injection for both the nominal engine.

	HTP / RP-1		NTO / N_2H_4
	1st plate	2nd plate	
ΔP fuel [bar]	-	5	8
ΔP oxidant [bar]	2	1	8
v_{fuel} [m/s]	-	24.6	27.9
$v_{oxidant}$ [m/s]	33.6	272.3 (Ma = 0.362)	23.3
N_{holes} fuel	-	38	82
N_{holes} oxidant	114	19	82
D_{inj} fuel	-	191 μm	192 μm
D_{inj} oxidant	0.3 mm	3.541 mm	192 μm
Inpingement type	Shower head	Triplet (gas in the middle)	Doublet (LIKE-LIKE)

Table 4.13: injector plate sizing for nominal engines

The fundamental parameters that have been chosen for the sizing of the injectors are the ΔP that the injection plate must give and the minimum hole diameter. For

the injection of the liquids the ΔP of the injection plate has been selected in order to have a velocity at the exit of the plate around 20 - 35 m/s and then guarantee a good atomization. At the contrary, the holes for the oxidant in gaseous form are design to avoid compressibility problem. However, has reported in Table 4.13 the mach number of oxidant after the plate is slightly above the compressible limit, therefore a more refinement analysis must be done considering that behaviour. At this stage the flow has been considered as incompressible. For the plate before the catalytic bed it has not been considered the additive manufacturing technique for its production. Therefore, the holes with a diameter of 0.3 mm has been adopted.

In a second step analysis, it has been considered the change of the propellant density due to the cooling system. In Table 4.14 are reported the results only for the *toxic* engine due to lack of data on the density variation with temperature and pressure of the *green* couple. In order to do not change the number of holes, the diameter of them has been increased.

	NTO/N_2H_4	
	fuel	**oxidant**
D_{inj}	210 μm	204 μm
% variation	9.8%	6.3%

Table 4.14: Size change due to density variation of the propellant (only nominal "toxic" engine)

4.4.2   Injector pattern

In order to achieve a uniform combustion, it is of upmost importance to distribute the injectors so that they are not clumped together, creating unstable combustion conditions which can lead to a rapid unscheduled structural problems. The number of injector elements and their sizing was determined as explained in Section 4.4.1. An example of injector pattern for *toxic* engine is presented in Figure 5.1; there are visible the injectors doublets and an additional ring of injectors for possible film cooling (not use in the designed engine).

4.5   Feeding system

From the high level requirements, suitable feeding systems following a standard pressure-fed architecture were designed. Furthermore, the systems will have totally separate tanks, feeding lines, check and latch valves for the oxidizer and the propellant. Figure 4.3 shows a generic schematics of the proposed architecture:
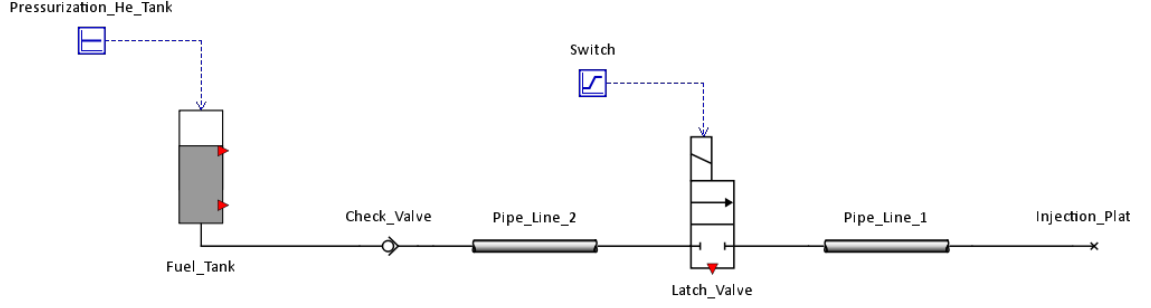
Figure 4.3: Feeding System Architecture's Schematics

4.5.1 Pipes pressure loss modelling

Due to its reliability, wide availability and compatibility with Hydrazine and Nitrogen Tetroxide [18], AISI 304 commercial pipes of diameters 1/8", 1/4" and 3/8" were selected. Each diameter was selected based on commercial availability and to allow flow velocities between 1 and 10 m/s. Table 4.15 displays the final relation of diameters to each engine feeding line and the respective flow velocity obtained for the desired chamber pressure ($1\ MPa$). An initial standardized length of $1\ m$ was selected.

The pressure inside the feeding line pipes was modelled using the Fanning Equation for flows inside circular pipes [39]:

$$\Delta P = \frac{2f\rho v^2 L}{D} \tag{4.1}$$

Where ρ is the fluid's density, L is the pipe's length, v is the flow's velocity inside the pipe, D is the pipe's diameter and f is known as the friction coefficient.

Since all Reynolds Numbers found place the designed flows inside the turbulent flow region on the Moody Diagram [39] (above $Re = 4000$) and the pipes' relative roughnesses (RPR) are sufficiently small, f was computed using the equation for smooth pipes for turbulent flow:

$$f = \frac{0.316}{Re^{1/4}} \tag{4.2}$$

The only exception for which using the above equation would not be as much suitable is the case of the downscaled toxic propellant engine, that has a flow of $Re = 2.5 \cdot 10^3$ inside the fuel's pipe. This value lies around the transition range, inside which a refined analysis requires a rather complex modelling. In conclusion, knowing that assuming turbulent flow implies in higher pressure losses, keeping the procedure adopted for the analysis of the other cases to this particular one implies on a conservative approach and will be the one selected for this preliminary design. A summary on the selected pipes, its respective diameters, Reynolds Numbers, friction coefficients and pressure losses are contained on Table 4.15.

Propellant	NTO / N_2H_4			HTP / RP-1		
Thrust Level	250 N	500 N	1000 N	250 N	500 N	1000 N
Pipe Diameter oxidant [mm]	3.175	6.35	9.525	6.35	9.525	9.525
Pipe Diameter fuel [mm]	3.175	6.35	9.525	3.175	3.175	6.35
v_{ox} [m/s]	1.74	3.48	1.55	1.1	3.8	7.61
v_{fuel} [m/s]	2.09	4.08	1.86	1.64	3.82	1.73
Re_{ox}	$1.64 \cdot 10^4$	$1.64 \cdot 10^4$	$2.19 \cdot 10^4$	$7.77 \cdot 10^3$	$4.15 \cdot 10^4$	$8.29 \cdot 10^4$
Re_f	$2.78 \cdot 10^4$	$2.85 \cdot 10^4$	$3.8 \cdot 10^4$	$2.52 \cdot 10^3$	$5.87 \cdot 10^3$	$5.32 \cdot 10^3$
f_{ox}	0.028	0.028	0.026	0.034	0.022	0.019
f_f	0.024	0.024	0.023	0.044	0.036	0.037
ΔP_{ox} [Pa]	$3.08 \cdot 10^5$	$3.84 \cdot 10^4$	$1.88 \cdot 10^4$	$1.74 \cdot 10^4$	$9.63 \cdot 10^4$	$3.24 \cdot 10^5$
ΔP_f [Pa]	$2.59 \cdot 10^5$	$3.38 \cdot 10^4$	$1.66 \cdot 10^4$	$6.12 \cdot 10^4$	$2.68 \cdot 10^5$	$2.83 \cdot 10^4$

Table 4.15: Pipe diameters, flow velocities, Reynolds Numbers, friction factors and pressure drop inside pipes.

4.5.2 Dynamic pressure loss modelling

Knowing the flow velocities inside the pipes, shown in Table 4.15, it is possible to size the amount of pressure that will be converted from static to kinetic from the tanks in order to accelerate the fluid into the pipes using the following equation:

$$\Delta P_k = \frac{1}{2}\rho v^2 \qquad (4.3)$$

Hence, knowing the densities of N_2O_4 (1448 kg/m^3), N_2H_4 (1008 kg/m^3), H_2O_2 (1430 kg/m^3) and RP-1 (807 kg/m^3), Table 4.16 presents the dynamic pressure drops expected for each designed system.

Propellant	NTO / N_2H_4			HTP / RP-1		
Thrust Level	250 N	500 N	1000 N	250 N	500 N	1000 N
$\Delta P_{k\,ox}$ [Pa]	$8.75 \cdot 10^3$	$2.19 \cdot 10^3$	$1.73 \cdot 10^3$	$8.19 \cdot 10^2$	$1.03 \cdot 10^4$	$4.14 \cdot 10^4$
$\Delta P_{k\,f}$ [Pa]	$8.40 \cdot 10^3$	$2.21 \cdot 10^3$	$1.75 \cdot 10^3$	$1.09 \cdot 10^3$	$5.90 \cdot 10^3$	$1.21 \cdot 10^3$

Table 4.16: Dynamic pressure drops for each system.

## 4.5.3 Valve decision and pressure drop modelling

Regarding the valve selection, two valves were selected, both from *VACCO Industries*: the 3/8" Low Pressure Check Valve V1D10856-02 and the 3/8" Low Pressure Propellant Latch Valve V1E10453-01. Both of them have been produced specifically for space applications and have maximum operating pressures above the ones obtained for the feeding system (56 bar [40] and 51 bar [41], correspondingly).

The choice for selecting valves with only one port diameter is justified due to the difficulty on picking valves that are flight proven, provide the necessary information for the proposed modelling of the produced pressure drop and are able to sustain the expected operating pressures. Besides, the compatibility problem may be avoided by using adapters,

which, for this preliminary analysis, may be considered frictionless and, therefore, would not contribute for the pressure loss. Hence, for preliminary modelling purposes, the choice is adequate.

(a) 3/8" Check Valve V1D10856-02
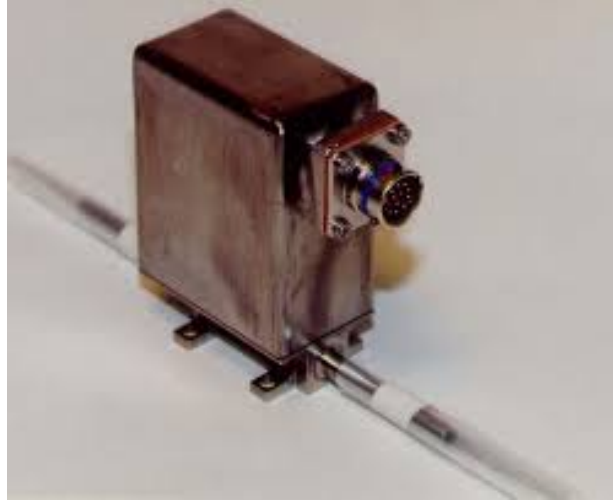
(b) 3/8" Latch Valve V1E10453-01

Figure 4.4: Selected valves

According to information of pressure drop as a function of the flow rate of water contained on the respective valves' brochures [40] [41], it is possible to derive the k factor for each one of them:

$$\Delta P = 0.5 \cdot k \rho v^2 \quad \Rightarrow k_{check} = 2.552 \quad ; \quad \Rightarrow k_{latch} = 40.289 \tag{4.4}$$

Finally, Table 4.17 contains all values obtained for the pressure drops caused by the passage of the flow through the valves, associated with the according valve and propulsive system.

Propellant	NTO / N_2H_4			HTP / RP-1		
Thrust Level	250 N	500 N	1000 N	250 N	500 N	1000 N
ΔP_{ox} check valve [Pa]	$2.23 \cdot 10^4$	$5.58 \cdot 10^3$	$4.41 \cdot 10^3$	$2.09 \cdot 10^3$	$2.64 \cdot 10^4$	$1.06 \cdot 10^5$
ΔP_f check valve [Pa]	$2.14 \cdot 10^4$	$5.63 \cdot 10^3$	$4.46 \cdot 10^3$	$2.78 \cdot 10^3$	$1.51 \cdot 10^4$	$3.10 \cdot 10^3$
ΔP_{ox} latch valve [Pa]	$3.53 \cdot 10^5$	$8.81 \cdot 10^4$	$6.96 \cdot 10^4$	$3.30 \cdot 10^4$	$4.17 \cdot 10^5$	$1.67 \cdot 10^6$
ΔP_f latch valve [Pa]	$3.38 \cdot 10^5$	$8.89 \cdot 10^4$	$7.03 \cdot 10^4$	$4.39 \cdot 10^4$	$2.38 \cdot 10^5$	$4.89 \cdot 10^3$

Table 4.17: Pressure drops associated with the valves for each system.

4.5.4 Injection plates and catalytic bed pressure drop modelling

The pressure drop over the injection plates was one of the input parameters that were defined *a priori* of the feeding system's design, Table 4.13 presents the assumed values.

Beyond that, for the specific case of the engines that use H_2O_2 as oxidant, an additional pressure drop, of $\Delta P = 9\ bar$ [42], due to the presence of the catalytic bed was considered. Also, because of the addition of this component, two injection plates were used and, therefore, two injection pressure drops were considered.

4.5.5   Cooling system pressure loss modelling

For the modelling of the pressure loss due to the redirecting of the propellant to the cooling system's channels an estimation of a drop of around 25% [43] of the combustion chamber's pressure, that is, 2.5 bar for all cases.

4.5.6   Pressure cascade and tank pressurization

By summing the defined Combustion Chamber pressure ($P_c = 1\ MPa$) to the calculated losses, it was possible to estimate the necessary pressurization inside the oxidant and fuel's tanks. Final results are displayed on Table 4.18.

Propellant	NTO / N_2H_4			HTP / RP-1		
Thrust Level	250 N	500 N	1000 N	250 N	500 N	1000 N
$P_{tank_{ox}}[bar]$	27.41	21.84	21.44	25.03	29.99	45.89
$P_{tank_f}[bar]$	26.77	21.81	21.43	18.59	22.77	18.31

Table 4.18: Expected required pressure inside tanks.

4.5.7   Pressurant sizing

After determining the propellant storage pressure, the pressurant gas mass was determined by using the conservation of energy in an adiabatic flow. Additionally, the initial pressurant pressure was determined by multiplying the highest propellant storage pressure by 10, ensuring that the propellants are sufficiently fed through the cooling and injection systems into the combustion chamber [44]; therefore the results reported in Table 4.19 represent a first estimation of mass, volume and pressure of the pressurant gas (Helium).

Propellant	NTO / N_2H_4			NTO / RP-1		
Thrust level	250 N	500 N	1000 N	250 N	500 N	1000 N
Mass [kg]	1.96	1.58	1.55	1.67	2.01	2.80
Volume [l]	44.2	44.8	44.8	41.2	41.4	37.8
Pressure [MPa]	27.4	21.8	21.4	25.0	30.0	45.9

Table 4.19: Mass, volume and initial pressure of the pressurant gas for each engine (upscale and downscaled included)

4.6   Final dimensions

The CAD model of the engine was constructed using Autodesk Inventor, which allows for parametric modelling. This was very useful when making the model of the nozzle and throat, both of which use equations that describe the contour of the bell-shaped nozzle

that can be plugged into Inventor. Figure 5.3 shows the internal shape of the engine case and its general dimensions [1].

		NTO / N2H4			HTP / RP - 1		
		250 N	500 N	1000 N	250 N	500 N	1000 N
ε_c	[-]	5.77	5.77	5.77	5.83	5.83	5.83
ε	[-]	200	200	110	200	200	110
L_c	[mm]	131.69	131.57	131.39	197.71	197.59	197.42
D_c	[mm]	31.43	44.45	62.86	31.07	43.94	62.14
D_t	[mm]	13.08	18.50	26.16	12.87	18.20	25.74
D_e	[mm]	185.01	261.64	274.41	182.00	257.38	269.94
L_{noz}	[mm]	224.57	317.59	324.26	220.92	312.42	318.99
$\dot{m}_p$	[g/s]	75.62	151.23	302.47	78.77	157.54	315.08
$\dot{m}_{p_{ox}}$	[g/s]	39.78	79.56	159.12	67.69	135.38	270.76
$\dot{m}_{p_{fuel}}$	[g/s]	35.84	71.67	143.35	11.08	22.16	44.32
T_{real}	[N]	245.5	491.1	982.3	245.6	491.2	982.4
Real $I_{s_{vac}}$	[s]	331.0	331.0	331.1	317.8	317.8	317.8
Burn time	[s]	3833	1917	958	3903	1951	976
Total I_s	[Ns]	941297	941297	941297	958474	958474	958474
m_p	[kg]	290	290	290	307	307	307
m_f	[kg]	137	137	137	43	43	43
m_{ox}	[kg]	152	152	152	264	264	264
$N_{inj_{fuel}}$	[-]	40	82	116	18	38	78
$N_{inj_{ox,l}}$	[-]	40	82	116	57	114	228
$N_{inj_{ox,g}}$	[-]	-	-	-	9	19	39
$D_{inj_{fuel}}$	[μm]	192	192	191	193	191	191
$D_{inj_{ox,liq}}$	[μm]	194	192	190	300	300	300
$D_{inj_{ox,gas}}$	[mm]	-	-	-	3.638	3.541	3.495

Table 4.20: Final parameter for all the engines considered

---

[1]For the green engines, the length of the combustion chamber include also the catalytic chamber ($35mm$)

Chapter 5

Conclusion

In the Table 4.20 a general comparison between the six engines is reported. Due to the lower Specific Impulse the propellant masses for the *green* couple is higher than the one of the *toxic* one.

The *green* propellant couple needs the addition of a catalytic bed in order to react properly. This leads to additional weight for the engine and an increased length of the combustion chamber. The presence of two injection plates increases the manufacturing complexity and the pipeline pressure. More over the gaseous flow after the catalytic bed needs an appropriate design of the second injection plate.

Both the engines are fully realizable in additive manufacturing. Also the divergent part of the nozzle in *Tantalum alloy* and the TBC can be 3D printed. For the *green* propellant engine the catalytic bed is compatible with additive techniques.

For the cooling performance evaluation are adopted some conservatives hypothesis, first of all the lower maximum temperature of the propellants, limited at ambient pressure. Considering a higher temperature on the external wall, due to the higher pressure, the constraints might be relaxed. The *green* propellant engine cooling performances are higher due to the high mass flow rate of oxidizer, capable of large heat absorption. For the two engines no cooling channels are designed, only a preliminary analysis on the partition of the cooled areas and the sizing of the TBC thickness is realized. The sizing of the cooling channels might change the presented results, according to the flow velocity in the channels.

Regarding the feeding line system, a final architecture with reasonable tank pressures was achieved for each design. However, it is noteworthy that: (1) the *green* propellant systems presented higher final tank pressures than their *toxic* counterparts (due to the addition of the catalytic bed) and, therefore, will present heavier architectures; (2) with the exception of the nominal engine designs, the values of flow velocities inside the pipes were found to be close to the bottom value expected of 1 m/s, which may translate into hydraulic response problems.

Increasing the thrust level the requested manoeuvre is realized in a shorter time, however the size of the engine increases. The fixed expansion ratio of 200:1, leads to an exit diameter no more compatible with the printable envelope. The higher thrust engine can be cooled more easily with respect to the one with half of the thrust. In fact the low mass flow rate in the small engine leads to cooling issues that should be solved using a different technique such as film cooling.

25

Bibliography

[1] *kick stage*. DOI: 10.1093/oi/authority.20110803100036169. URL: https://www.oxfordreference.com/view/10.1093/oi/authority.20110803100036169.

[2] Aerojet Rocket Liquid Company. "ARIES Kick stage". In: (1977).

[3] Skyrora. "Payload User's Guide, Skyrora XL". In: (2019).

[4] RocketLab. "Payload User's Guide, Electron". In: (2022).

[5] L Ordonez Valles et al. "Challenges and opportunities of green propellants and electric pump feeding for future European kick stages". In: *Aerotecnica Missili & Spazio* (2022), pp. 1–15.

[6] Aerojet Rocketdyne. "Bipropellant Propulsion, https://satcatalog.s3.amazonaws.com/components/1017/SatCatalog_-_Aerojet_Rocketdyne_-_R-4D-15_HiPAT_445N_High_Performance_375-to-1_-_Datasheet.pdf?lastmod=20210710071031". In: ().

[7] IHI AeroSpace. "Bipropellant Thrusters, https://satcatalog.s3.amazonaws.com/components/1271/SatCatalog_-_IHI_Aerospace_-_BT-4_-_Datasheet.pdf?lastmod=20211008050540". In: ().

[8] ArianeSpace. "Chemical bipropellant thruster families, https://www.space-propulsion.com/brochures/bipropellant-thrusters/bipropellant-thrusters.pdf". In: ().

[9] Stefania Carlotti and Filippo Maggi. "Evaluating New Liquid Storable Bipropellants: Safety and Performance Assessments". In: *Aerospace* 9.10 (2022), p. 561.

[10] Wolter Wieling Alfons Mayer. "GREEN PROPULSION RESEARCH". In: (2018), p. 28.

[11] Wojciech Florczuk and Grzegorz Rarata. "Assessment of various fuel additives for reliable hypergolic ignition with 98%+ HTP". In: (2015).

[12] Joe W Magee et al. "Thermophysical properties measurements and models for rocket propellant RP-1: Phase I". In: (2007).

[13] Sungyong An Sungkwon Jo Sejin Kwon. "Performance Characteristics of Hydrogen Peroxide/Kerosene Staged-Bipropellant Engine with Axial Fuel Injector". In: (2011), p. 9.

[14] Simon Reid et al. "Towards an advanced 3D-printed catalyst for hydrogen peroxide decomposition: Development and characterisation". In: (2023), p. 15.

[15] Suraj Rawal, James Brantley, and Nafiz Karabudak. "Additive manufacturing of Ti-6Al-4V alloy components for spacecraft applications". In: *2013 6th international conference on recent advances in space technologies (RAST)*. IEEE. 2013, pp. 5–11.

[16] Paul Gradl, Omar Mireles, and Nathan Andrews. "Intro to additive manufacturing for propulsion systems". In: *AIAA Joint Propulsion Conference*. M18-6849. 2018.

[17] Peng-Hui Li et al. "Thermomechanical response of 3D laser-deposited Ti–6Al–4V alloy over a wide range of strain rates and temperatures". In: *Materials Science and Engineering: A* 647 (2015), pp. 34–42.

[18] Robert Lechler. "Revised Version-"Literature Survey of Materials compatible with Propellants" Additive Manufacturing Based Bellows Working Package 1: Selection of a suitable Material and Process Combination". In: (2015).

[19] Paul R Gradl et al. "Additive manufacturing of liquid rocket engine combustion devices: a summary of process developments and hot-fire testing results". In: *2018 Joint propulsion conference*. 2018, p. 4625.

[20] Limited Aeether Co. *Inconel alloy 625 vs Inconel alloy 718 [compare from 10 aspects]*. URL: https://www.aeether.com/AEETHER/media/media-33/media.html.

[21] Zhihua Tian et al. "A review on laser powder bed fusion of inconel 625 nickel-based alloy". In: *Applied Sciences* 10.1 (2019), p. 81.

[22] *Large Format Selective Laser Melting*. Tech. rep. SLM Solutions Group AG.

[23] UltiMaker. *UltiMaker Cura*. Version 5.3.0. Apr. 20, 2023. URL: https://ultimaker.com/software/ultimaker-cura.

[24] SLM Solutions. *Material Data Sheet Ni-Alloy IN625 / 2.4856 / B446*. Tech. rep.

[25] A Lynam et al. "Thermal spraying of ultra-high temperature ceramics: A review on processing routes and performance". In: *Journal of Thermal Spray Technology* 31.4 (2022), pp. 745–779.

[26] Brian Reed, James Biaglow, and Steven Schneider. "Advanced materials for radiation-cooled rockets". In: *Pennsylvania State Univ., NASA Propulsion Engineering Research Center, Volume 2* (1993).

[27] Roxana Family and M Pinar Mengüç. "Analysis of sustainable materials for radiative cooling potential of building surfaces". In: *Sustainability* 10.9 (2018), p. 3049.

[28] Materion. *Niobium C-103 Alloy for Space Exploration*. 2022. URL: https://materion.com/-/media/files/alloy/datasheets/other-alloy-products/niobium-c103-alloy-for-space-data-sheet.pdf.

[29] VP Babak et al. "Thermal barrier coatings on niobium-based alloys structural materials". In: (2019).

[30] Xu Zhang et al. "The protection, challenge, and prospect of anti-oxidation coating on the surface of niobium alloy". In: *Coatings* 11.7 (2021), p. 742.

[31] Brian D Reed, James A Biaglow, and Steven J Schneider. "Iridium-coated rhenium radiation-cooled rockets". In: *NASA-TM-107453* (1997).

[32] Nenad D Milošević et al. "Thermal properties of tantalum between 300 and 2300 K". In: *International journal of thermophysics* 20 (1999), pp. 1129–1136.

[33] Dongwook Jang, Youngchul Kwak, and Sejin Kwon. "Design and validation of a liquid film-cooled hydrogen peroxide/kerosene bipropellant thruster". In: *Journal of Propulsion and Power* 31.2 (2015), pp. 761–765.

[34] NASA. *Liquid Rocket Engine Nozzles, SP-8120*. Tech. rep. NASA, July 1976.

[35] G.V.R. Rao. "Exhaust Nozzle Contour for Optimum Thrust". In: *AIAA Jet Propulsion* 28.6 (June 1958), pp. 377–382.

[36] Dieter K Huzel and David H Huang. *Design of liquid propellant rocket engines*. Tech. rep. 1967.

[37]   Robert D McCarty, Hans-Ulrich Steurer, and CM Daily. *The Thermodynamic Properties of Nitrogen Tetroxide.* US Department of Commerce, National Bureau of Standards, 1986.

[38]   G. S. Gill and W. H. Nurick. *Liquid Rocket Engine Injectors, SP-8089.* Tech. rep. NASA, Mar. 1976.

[39]   Lewis F Moody. "Friction factors for pipe flow". In: *Transactions of the American Society of Mechanical Engineers* 66.8 (1944), pp. 671–678.

[40]   VACCO Industries Space Products. *3/8" LOW PRESSURE CHECK VALVE V1D10856-02.* Tech. rep., pp. 1–2.

[41]   VACCO Industries Space Products. *3/8" LOW PRESSURE PROPELLANT LATCH VALVE V1E10453-01.* Tech. rep., pp. 9–10.

[42]   Shinjae Kang. "Catalyst bed behavior of hydrogen peroxide/kerosene bipropellant thruster in monopropellant and bipropellant modes with cavitating venturi valve". In: *Acta Astronautica* 205 (2023), pp. 47–56.

[43]   Filippo Maggi. "LRE Technology". In: *Politecnico di Milano* (2022-2023), p. 53.

[44]   Lavagna Michèle Roberta. "Propulsion subsystmem". In: *Politecnico di Milano* (2022-2023), p. 35.
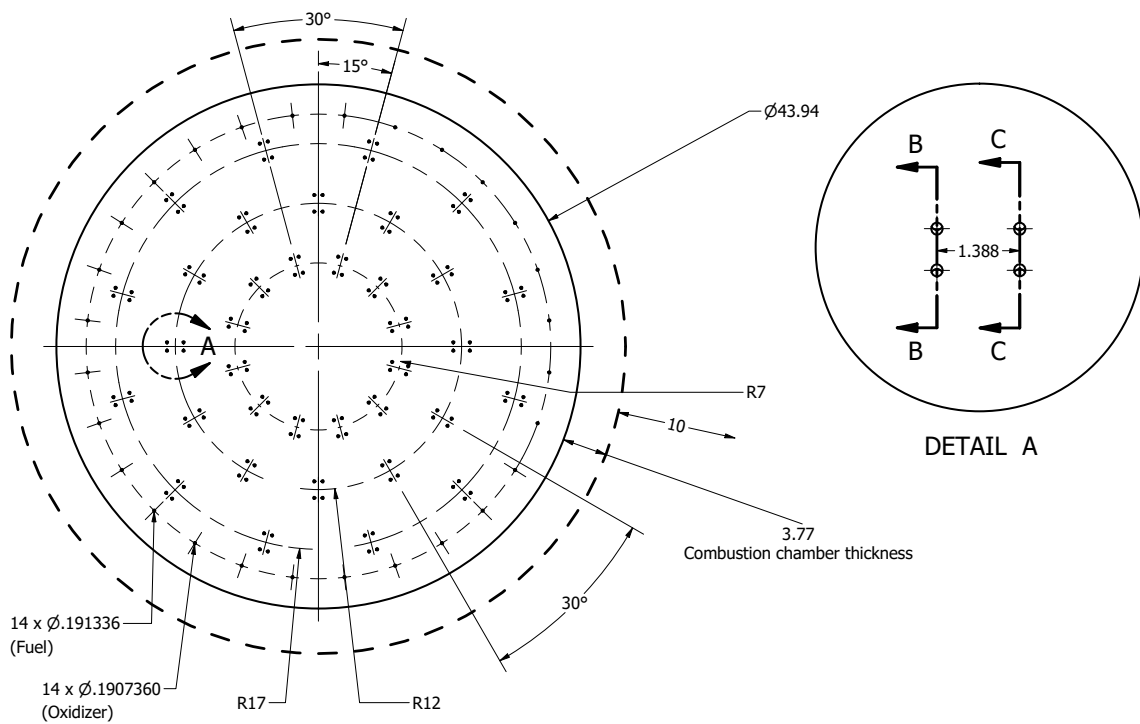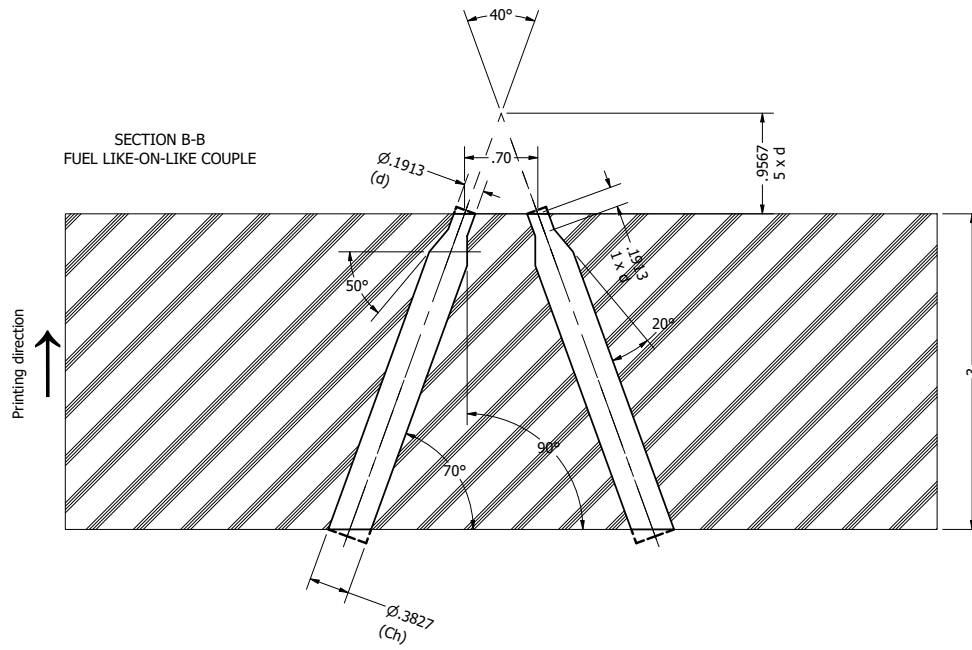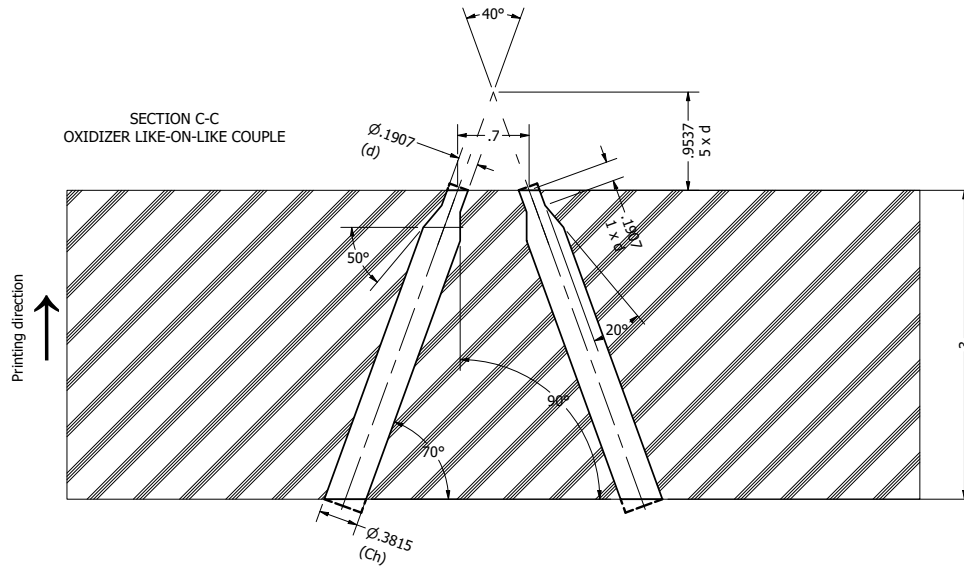
Appendix

Injector plate

Figure 5.1: Injector plate dimensions and geometry for the NTO-Hydrazine propellant couple

(a) Fuel injector section view

(b) Oxidizer injector section view

Figure 5.2: Injector hole design and dimensions for the NTO-Hydrazine propellant couple
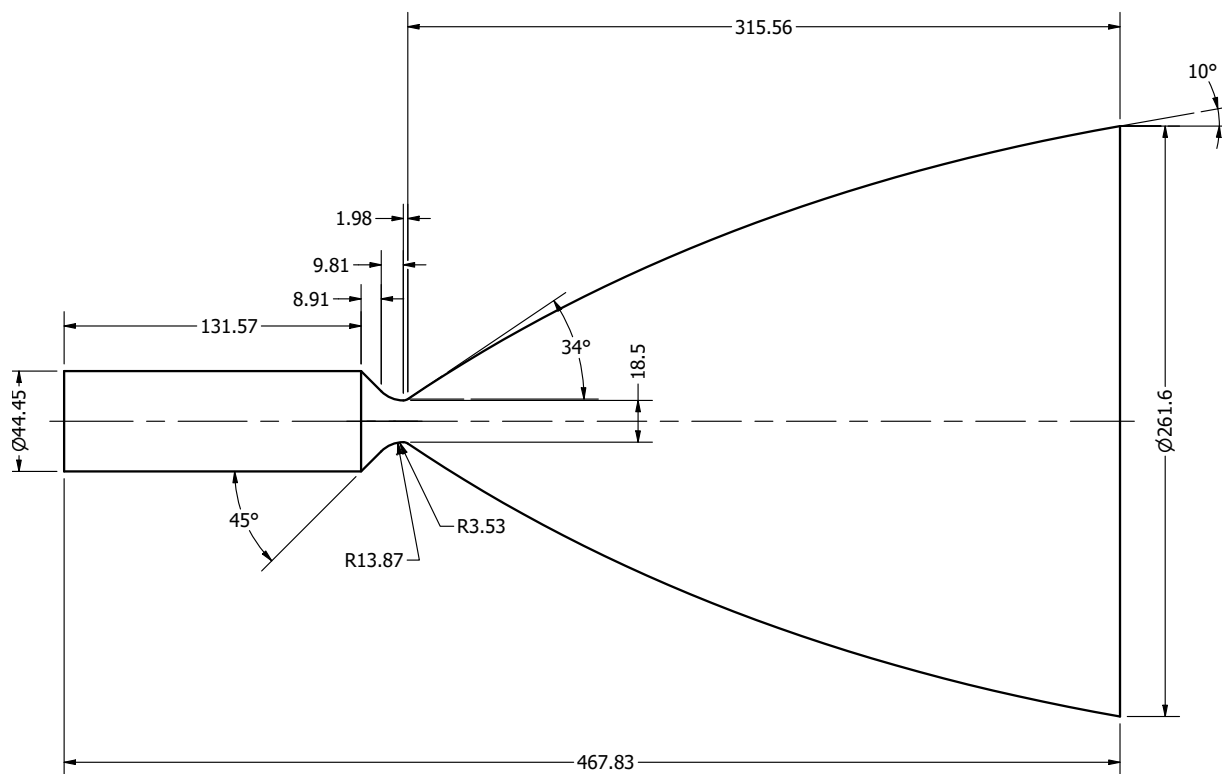
2D drawings

Figure 5.3: Internal dimensions of the combustion chamber, throat and nozzle for the 500N-thrust engine